Numerical modelling and in-situ experiment for self-sealing of the induced fracture network of drift into the Callovo-Oxfordian claystone during a hydration process

Hui Wang, Rémi de La Vaissière, Minh-Ngoc Vu, Christian La Borderie, Domenico Gallipoli

Numerical modelling and in-situ experiment for self-sealing of the induced fracture network of drift into the Callovo-Oxfordian claystone during a hydration process

Hui Wang[a,b,*], Rémi de La Vaissière[c], Minh-Ngoc Vu[c] , Christian La Borderie[b], Domenico Gallipoli[b]

[a]*School of Civil and Architectural Engineering, Hainan University, Hainan, China*

[b]*Université de Pau et des Pays de l'Adour, Département de génie civil, SIAME, Allée du Parc Montaury, 64600 Anglet, France*

[c]*Andra, 1-7, rue Jean Monnet, 92298 Chatenay-Malabry, France*

Abstract.

The excavation damage zone surrounding an underground tunnel/gallery, and in particular its evolution, is being studied for the performance assessment of a radioactive waste underground repository. This paper focuses on numerical analysis of the self-sealing of the damaged zone based on an in-situ CDZ experiment for exploring the self-sealing of excavation damage zone during a hydration process. A plastic damage model is employed to describe the mechanical behaviour of Callovo-Oxfordian claystone (COx), and an added deformation model coupled with the standard Biot's model to simulate the significant deformation of COx claystone during the change of water content. Crack estimation and permeability evaluation of unsaturated fractured COx claystone are carried out through a post-processing method based on the fracture energy regularization and the cubic law, respectively. The validation of the proposed model is performed by numerical simulation of: (1) COx claystone swelling and triaxial compression tests， (2) self-sealing of fractured COx claystone samples during hydration process, (3) self-sealing of the damaged zone during a hydration process. Comparisons between the numerical and experimental results demonstrate the reliability of the proposed model to accurately describe the self-sealing of the fractured COx claystone, and the global water permeability reduction in hydration illustrates the accomplishment of the self-sealing of damaged zone.

Keywords: Self-sealing, COx claystone, damaged zone, numerical modeling, in-situ experiment, permeability.

1. Introduction

In France, Callovo-Oxfordian claystone, in its natural state, exhibits excellent conditions for the storage of radioactive waste thanks to its signigicant retention capacity for radionuclides, small molecular diffusion and low permeability (Descostes et al., 2008). Therefore, deep geological disposal for intermediate level long-life radioactive waste (IL-LLW) and high-level radioactive waste (HLW) called Cigéo is planned to be constructed in deep Callovo-Oxfordian claystone (COx) formation (~150 m thickness), and Cigéo will be in the middle of the COx claystone formation (around ~500 m deep). Since 2000, to conduct experiments and to be able to validate the feasibility of establishing and operating a nuclear waste disposal facility in Callovo-Oxfordian claystone, Andra launched the construction of the Meuse Haute-Marne underground laboratory (Andra, 2005). The laboratory,mainly located at 490 m below the ground, is accessible by means of two vertical shafts dug. Along with the vertical shafts digging and underground tunnels excavation, a drying process of the COx claystone close to the excavation surface is occurring caused by the ventilation of the shafts and tunnels (Armand et al. 2014; de La Vaissière et al., 2015). The loss of water by the ventilation makes water saturation of COx claystone decrease from 100% to 70% within a distance of 0 m – 1 m from the exposed surface. The underground tunnels excavating, the desaturating of the COx claystone, and the associated increasing of pore water tension, control the shrinkage of the material and the consequent reduction of total stresses in radius direction of underground drifts (Diederichs, 2003; Vinsot et al., 2014). This decompression also causes the development of fractures of different sizes close to the excavated area, which increases permeability of this zone (Armand et al. 2014; de La Vaissière et al., 2015, Pardoen et al., 2016). As evidenced by Armand et al. (2014), excavation of COx claystone within the URL provokes fractured zone due to (1) the anisotropy of in-situ stress state (Wileveau et al., 2007); (2) inherent anisotropy of material (elasticity, strength, permeability, etc.) (Armand et al., 2017; Zhang et al., 2019) and (3) induced anisotropy (pore pressure distribution, damage instability, etc.) (Trivellato et al., 2019; Souley et al., 2020; Vu et al., 2020). The excavation induced fractured zone includes the zone of connected fractures (more frequently referred to as excavated damage zone), containing both extensional and shear fractures as well as the zone of diffuse fractures containing only shear fractures (Armand et al., 2014). The permeability of intact COx claystone is about $10^{-20}\ m^2$ (de La Vaissière et al., 2015; Giot et al., 2018). In the zone of connected fractures, cracks develop from the surrounding rock surface and tend to be larger generating values of permeability up to $10^{-17} m^2$. Instead, in the zone of diffuse fractures, which is between the connected fractured zone and the intact rock, permeability remains relatively low, i.e. between $10^{-19} m^2$ and

$10^{-17}m^2$. An increase of permeability in both zones augments the risk of radionuclide leakage, which can be mitigated by the self-sealing of the COx claystone upon resaturation.

As shown in many experimental studies, the swelling property of the COx claystone during resaturation similarly displayed in other claystone (Qi and Vanapalli, 2016; Li et al., 2016; Zhou et al., 2017; Gong and Chok, 2018; Liu and Vanapalli, 2019; He et al, 2020; Souza and Pejon, 2020), and the swelling of the COx claystone is significant to seal the fractures of the damage zone (Pham et al., 2007; Davy et al., 2007; Zhang, 2013). In laboratory tests, the free volumetric swelling of the COx claystone by hydration was beyond 8% in comparison with samples's original volume, and its significant capacity of swelling during wetting processes were observed even the confining pressure reached 17 MPa (Zhang, 2013, Zhang et al., 2020). In self-sealing experiments of fractured COx claystone, the permeability of fractured COx samples can be more than the level of $10^{-10}\mathrm{m}^2$, however, the permeability can reduce to less than the level of $10^{-17}\mathrm{m}^2$ after a hydration process, and the main reason led to this reduction is due to the significant swelling of the COx claystone meeting water.

The self-sealing of the damaged zone in drifts and shafts is crucial to the safety of underground nuclear waste disposal. Due to the swelling capacity of bentonite during a resaturation process, it has been chosen as the main element of the sealing system (Assadollahi and Nowamooz, 2020; Darde et al., 2020). A swelling pressure from bentonite is provided against the walls of underground drifts, and this pressure helps to seal the damaged zone and recover galleries' radius stress. Between 2010 and 2012, CDZ (Compression of the Damaged Zone: a specific experiment) was carried out to study the evolution of the excavation damaged zone properties (fractures, permeability) upon the resaturation and the mechanical loading on the drift wall (de La Vaissière et al., 2014, 2015). The investigation results from CDZ experiments prove that the damaged zone can accomplish self-sealing upon both mechanical loading and resaturation, which is a key information for the safe storage of nuclear waste in underground galleries.

The application of numerical analysis is essential to understand the self-sealing of fractured COx claystone, at the same time, to validate a numerical tool for the long-term safety assessment of the underground disposal with accounting the self-sealing process. As far as the authors know, there wasn't an existed large-scale modelling of self-sealing of clay material under both the mechanical loadings and the resaturation yet. This is the main purpose and motivation of the research. To describe the hydro-mechanical behaviour of the COx claystone, a material model is formulated. The formulated model can analyse the fracturing of the unsaturated COx claystone upon excavation/desaturation, and also it is used to explain the self-sealing mechanism of the damaged zone. Gens and Alonso (1992), and a number of scientists have studied the hydro-mechanical behaviour of soils,

building up a framework to predict the unsaturated soils deformation upon suction changes. On the basis of these previous research, we develop a model in this paper that applies to the prediction of swelling/shrinkage of COx claystone caused by changes in water content. In terms of the COx claystone, it is made up by 40%-45% fine clay matrix, 20%-30% quartz and 20%-30% calcite grains (Conil et al., 2020), and its significant deformation behaviour and the self-sealing quality are primarily decided by the clay part. In addition, Nadai criterion is taken to compute the plastic behaviour of the COx claystone, and then crack estimation, permeability computation and water diffusion inside fractured COx claystone are carried out, respectively. Based on the numerical methods discussed above and experiments carried out (Davy et al., 2007; de La Vaissière et al., 2015), this paper focuses on the predictions of the self-sealing of cracked COx claystone samples and fractures connected zone by hydration.

2. Constitutive model

2.1 Mechanical model

2.1.1 Equilibrium equation

According to the Biot's theory, and with the stress calculated from the added deformation, the equilibrium equation is written as follows:

$$\boldsymbol{\sigma} = \boldsymbol{\sigma_e} + \mathrm{BS_eP_c}\mathbf{I} - 3\mathrm{K}\Delta\varepsilon_{\mathrm{added}}\mathbf{I} \tag{1}$$

which is the sum of the skeleton stress $\boldsymbol{\sigma_e}$, the capillary stress $\mathrm{BS_eP_c}\mathrm{I}$ (Assuming that the capillary pressure is equal to total suction, and the effect of solute suction is relatively small. However, several projects exploring the impacts of solute suction were carried out in Andra, and a better understanding on this point for the COx claystone can be provided in future) and the stress produced by the added deformation, where B is the Biot coefficient (the Biot coefficient B from Armand et al. (2017) is 0.85 for the COx claystone). K is the Bulk Modulus. The term F in equation (2) represents the body force.

$$\mathbf{div}(\boldsymbol{\sigma}) + \mathbf{F} = \mathbf{0} \tag{2}$$

2.1.2 Parameters of unsaturated COx

Based on our previous works refer to Young Modulus E, tensile stress σ_t and fracture energy G_f of the COx claystone (Wang et al., 2020), here the relations between these three parameters and capillary pressure are directly listed in the following equations, respectively, which are used in numerical simulation afterwards.

$$\mathrm{E} = \left(-1.09 \times e^{\frac{W_w P_c}{RT\rho_w}} + 2.04\right) E_{\_saturated} \tag{3}$$

$$\sigma_t = \sigma_{t0}\left(1 + \sqrt{\frac{P_c}{P_t}}\right) \tag{4}$$

$$G_f = G_{f0}(1 + \frac{P_c}{P_{gf}}) \quad (5)$$

where W_w, R, T, ρ_w are Molar mass of water, the universal gas constant, temperature and water density, respectively. The rested parameter values of the three equations above are listed in Table 1.

Table 1 Parameters for evolutions of σ_t, E, G_f with changing of water content

Parameters	σ_{t0}	P_t	G_{f0}	P_f	$E_{\_saturated}$
Values	$5.\times 10^5$Pa	-5.9×10^7Pa	6.4N/m	-4.8×10^7Pa	4.32×10^9 Pa

2.1.3 Plasticity and Yielding criterion

The following flow function $F(\bar{\boldsymbol{\sigma}})$ is introduced to define the plastic surface.

$$F(\bar{\boldsymbol{\sigma}}) = \frac{(\bar{\sigma}_v + B1*(\bar{\sigma}_x + \bar{\sigma}_y + \bar{\sigma}_z))}{C1} - (R0 + R) \quad (6)$$

where B1, C1, R0 and R are four material parameters with B1 and C1 being determined according to the Nadai plastic criterion, R0 being equal to tensile stress σ_t and $R = MP \cdot \boldsymbol{\varepsilon}^{\mathbf{p}}$ being plastic strain, MP being the plastic strain slope and its values is equal to 0.5 times the Young Modulus E and $\boldsymbol{\varepsilon}^{\mathbf{p}}$ is the plastic strain. σ_v is the Von Mises equivalent stress while B1 and C1 depend on the values of $\bar{\sigma}_x + \bar{\sigma}_y + \bar{\sigma}_z$. In particular, when $\bar{\sigma}_x + \bar{\sigma}_y + \bar{\sigma}_z > -4 \times (R0 + R)$, then B1=1 and C1=2, else B1=0.25 and C1=3. According to Hooke's law and using $\boldsymbol{\varepsilon}^{\mathbf{p}}$ calculated from plastic flow equation, the effective stress $\bar{\boldsymbol{\sigma}}_{\mathbf{ij}}$ after plastic deformation can be expressed as follows:

$$\bar{\boldsymbol{\sigma}}_{\mathbf{ij}} = \lambda(\boldsymbol{\varepsilon}_{\mathbf{kk}} - \boldsymbol{\varepsilon}^{\mathbf{p}}_{\mathbf{kk}})\delta_{ij} + 2G(\boldsymbol{\varepsilon}_{\mathbf{ij}} - \boldsymbol{\varepsilon}^{\mathbf{p}}_{\mathbf{ij}}) \quad (7)$$

where $\lambda = \frac{\upsilon E}{(1+\upsilon)(1+2\upsilon)}$ and $G = \frac{E}{2(1+\upsilon)}$, ε_{kk} and ε_{ij} are total strains, $\boldsymbol{\varepsilon}^{\mathbf{p}}_{\mathbf{kk}}$ and $\boldsymbol{\varepsilon}^{\mathbf{p}}_{\mathbf{ij}}$ are plastic strains. When i=j, $\delta_{ij} = 1$, else $\delta_{ij} = 0$. The Poisson ratio υ is 0.295 .

2.1.4 Damage model

The damage model is based on the continuum mechanics framework developed by Fichant et al. (1999) where the effective stress in the damaged material is related to the macroscopic stress. Here the damage model is coupled with a plastic model and equation (14) is formulated in terms of elastic strains $\boldsymbol{\varepsilon}^{\mathbf{e}}_{\mathbf{kk}} = \boldsymbol{\varepsilon}_{\mathbf{kk}} - \boldsymbol{\varepsilon}^{\mathbf{p}}_{\mathbf{kk}}$ and $\boldsymbol{\varepsilon}^{\mathbf{e}}_{\mathbf{ij}} = \boldsymbol{\varepsilon}_{\mathbf{ij}} - \boldsymbol{\varepsilon}^{\mathbf{p}}_{\mathbf{ij}}$ directly as follows:

$$\bar{\boldsymbol{\sigma}}_{\mathbf{ij}} = \lambda\boldsymbol{\varepsilon}^{\mathbf{e}}_{\mathbf{kk}}\delta_{ij} + 2G\boldsymbol{\varepsilon}^{\mathbf{e}}_{\mathbf{ij}} \quad (8)$$

while the effective stress $\boldsymbol{\sigma}^{\mathbf{e}}_{\mathbf{ij}}$ of the damage model is expressed as follows:

$$\boldsymbol{\sigma}^{\mathbf{e}}_{\mathbf{ij}} = (1 - d)\bar{\boldsymbol{\sigma}}^{+}_{\mathbf{ij}} + (1 - d^{\alpha 1})\bar{\boldsymbol{\sigma}}^{-}_{\mathbf{ij}} \quad (9)$$

where $\bar{\boldsymbol{\sigma}}_{\mathbf{ij}}^{+}$ is the tensile part of $\bar{\boldsymbol{\sigma}}_{\mathbf{ij}}$ and $\bar{\boldsymbol{\sigma}}_{\mathbf{ij}}^{-}$ is the compressive part. The symbol d indicates the damage variable (note that, in the isotropic version of the model, d is taken as a scalar) while $\alpha 1 = 15$. The evolution of the scalar damage variable follows the normality rule according to the following expression:

$$d = 1 - \frac{\varepsilon_{d0}}{\tilde{\boldsymbol{\varepsilon}}} \exp(\beta(\varepsilon_{d0} - \tilde{\boldsymbol{\varepsilon}})) \tag{10}$$

where ε_{d0} is the damage threshold and its value is equal to σ_t/E while, β is a hardening/softening variable. The parameter β commands the slope of the softening curve, and its relation with the fracture energy G_f is given below, where h is the size of mesh element:

$$G_f = h\frac{E*\varepsilon_{d0}}{\beta} \tag{11}$$

Finally, the equivalent strain $\tilde{\varepsilon}$ is defined as:

$$\tilde{\boldsymbol{\varepsilon}} = \sqrt{\boldsymbol{\varepsilon}_{\mathbf{I}}^{+\,2} + \boldsymbol{\varepsilon}_{\mathbf{II}}^{+\,2} + \boldsymbol{\varepsilon}_{\mathbf{III}}^{+\,2}} \tag{12}$$

where $\boldsymbol{\varepsilon}_{\mathbf{I}}^{+}$, $\boldsymbol{\varepsilon}_{\mathbf{II}}^{+}$ and $\boldsymbol{\varepsilon}_{\mathbf{III}}^{+}$ are the principal elastic strains.

2.1.5 Crack estimation

A practical finite element method has been developed to compute cracks on the basis of a damage plastic model developed by Matallah and La Borderie (2009), which is based on the fracture energy regularization. The crack openings evaluation concerns skeleton solid phase, and the total strain of the skeleton phase is as follows:

$$\boldsymbol{\varepsilon}_{\mathbf{kl}} = \mathbf{C}_{\mathbf{ijkl}}^{\mathbf{0}\,-1}\bar{\boldsymbol{\sigma}}_{\mathbf{ij}} \tag{13}$$

The effective strain of skeleton was obtained as follows:

$$\boldsymbol{\varepsilon}_{\mathbf{kl}}^{\mathbf{e}} = \mathbf{C}_{\mathbf{ijkl}}^{\mathbf{0}\,-1}\boldsymbol{\sigma}_{\mathbf{ij}}^{\mathbf{e}} \tag{14}$$

The total strain $\boldsymbol{\varepsilon}_{\mathbf{kl}}$ in the solid skeleton is decomposed into two parts: an elastic part $\boldsymbol{\varepsilon}_{\mathbf{ij}}^{\mathbf{e}}$ and a cracking part and, it is represented by the Unitary Crack Opening strain tensor $\boldsymbol{\varepsilon}_{\mathbf{ij}}^{\mathbf{uco}}$:

$$\boldsymbol{\varepsilon}_{\mathbf{ij}}^{\mathbf{uco}} = \boldsymbol{\varepsilon}_{\mathbf{kl}} - \boldsymbol{\varepsilon}_{\mathbf{ij}}^{\mathbf{e}} \tag{15}$$

Multiplying the unitary crack opening strain $\boldsymbol{\varepsilon}_{\mathbf{kl}}^{\mathbf{uco}}$ by the size of numerical element h, the width of the crack is obtained as follows:

$$\boldsymbol{\delta}_{\mathbf{n}} = \mathbf{n}_{\mathbf{i}}\boldsymbol{\delta}_{\mathbf{ij}}\mathbf{n}_{\mathbf{j}} = \mathbf{n}_{\mathbf{i}}h\boldsymbol{\varepsilon}_{\mathbf{kl}}^{\mathbf{uco}}\mathbf{n}_{\mathbf{j}} \tag{16}$$

where **n** is the unit vector normal to the crack, the method of crack estimation has been validated under different arbitrary loadings and complex boundary conditions.

2.2 Added deformation law

Fig.1 provides a comparison of the swelling/shrinkage of the COx claystone predicted by the Biot's model (Biot and M.A., 1941) during a cyclic variation of capillary pressure and the values measured by Zhang et al. (2010) during free deformation experiments.

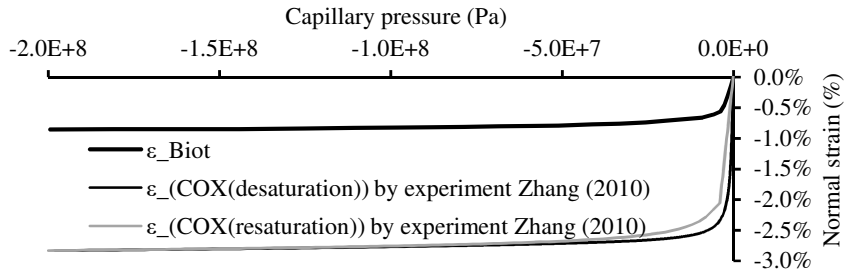

Fig. 1. Comparison of free swelling/shrinkage deformations

The initial saturation of a COx claystone sample and its corresponding capillary pressure are 0.9 and -14 MPa, respectively, in the experiment Zhang et al. (2010). Through flowing dry gas with a relative humidity 25% (capillary pressure -200MPa) on the sample for 30 days, after that, the dried sample was put into water (capillary pressure 0MPa), and the shrinkage and swelling of the COx sample were recorded during the drying and wetting processes. In Fig. 1., It is clear that the COx claystone deformation produced by the standard Biot's model is far less than that values measured from the experiments, therefore, a new law for calculating the extra wetting/drying deformations is added up with the standard Biot's model to match experimental data in this research. The added deformation model aims to reproduce the difference between the measured COx claystone desaturation and resaturation curves ($\varepsilon_{COX(desaturation)}$ and $\varepsilon_{COX(resaturation)}$ shown in Fig. 1) and the calculated standard Biot's curve (ε_{Biot} also shown in Fig. 1) (Wang et al., 2020):

$$\varepsilon^{exp}_{added(desaturation)} = \varepsilon_{COX(desaturation)} - \varepsilon_{Biot} = a_w \exp\left(\frac{b_w}{P_c}\right) \tag{17}$$

$$\varepsilon^{exp}_{added(resaturation)} = \varepsilon_{COX(resaturation)} - \varepsilon_{Biot} = a_k \exp\left(\frac{b_k}{P_c+\Delta p}\right) \tag{18}$$

where a_w, b_w, a_k, b_k and Δp are model parameters. The two above quations are then combined into a single equation as follows:

$$\varepsilon_{added(i)} = a_i \exp\left(\frac{b_i}{P_{c(i)}+\Delta P_i}\right) \tag{19}$$

where a_i, b_i and ΔP_i are model parameters. Derivation of the combined equation provides the added deformation slope $\frac{d\varepsilon_{added(i)}}{dP_{c(i)}}$ from which the strain differential is obtained as:

$$d\varepsilon_{added(i)} = \frac{d\varepsilon_{added(i)}}{dP_{c(i)}} dP_{c(i)} = \left(-\frac{a_i b \exp\left(\frac{b_i}{P_{c(i)}+\Delta P}\right)}{\left(P_{c(i)}+\Delta P\right)^2}\right) \times dP_{c(i)} \tag{20}$$

When capillary pressure increases from P_{c0} to P_c , $d\varepsilon_{added(i)}$ can be integrated within the range between P_{c0} and P_c, and then the strain increment is concluded as follows:

$$\Delta\varepsilon_{added} = \int_{P_{c0}}^{P_c} \frac{d\varepsilon_{added(i)}}{dP_{c(i)}} dP_{c(i)} \tag{21}$$

This added deformation model performed very well in numerical computation of COx claystone hydro-mechanical behaviour, and the details of the extra deformation law formulation can also be seen from Wang et al., (2020).

2.3 Permeability and Diffusion

As we know, the Darcy law performs very well in describe fluid flow through a non-fractured porous material. In the case that a porous material fractured, the Cubic law (Witherspoon, 1980) is used to describe flow through fractures, and as in the authors previous work Matallah and La Borderie (2016), the permeability matrix in principal coordinate expresses as follows:

$$\boldsymbol{\kappa} = \begin{bmatrix} \kappa_0 + \frac{\xi(w_3)w_3^3}{12L_3} + \frac{\xi(w_2)w_2^3}{12L_2} & 0 & 0 \\ 0 & \kappa_0 + \frac{\xi(w_3)w_3^3}{12L_3} + \frac{\xi(w_1)w_1^3}{12L_1} & 0 \\ 0 & 0 & \kappa_0 + \frac{\xi(w_2)w_2^3}{12L_2} + \frac{\xi(w_1)w_1^3}{12L_1} \end{bmatrix} \tag{22}$$

where w_1, w_2, w_3 are fracture values computed from the cracks estimation model, and ξ is an empirical coefficient to correct the standard cubic law as follows

$$\xi = \left(\frac{w}{w_f}\right)^{\gamma} \quad \text{if } w < w_f \tag{23}$$

here this equation is directly used for the Callovo-Oxfordian claystone with $w_f = 278\mu m$ and $\gamma = 1.45$. Based on the previous work by Fachy et al. (2013), introducing Darcy law into the water balance equation, the differential relation can be obtained as follows:

$$c\frac{\partial P_c}{\partial t} - \frac{k}{g} div\left(\nabla(P_c - pgz)\right) = 0 \tag{24}$$

where P_c is capillary pressure field changing with time, and c is the mass capacity which is written as follows:

$$c = -\rho\frac{\partial\theta}{\partial P_c} \tag{25}$$

where ρ is water density. According to Vogel et al. (2000), a modified Van Genuchten's retention model is proposed, and θ is written as follows:

$$\theta = \begin{cases} S_e(\theta_s - \theta_r) + \theta_r & \text{if } P_c > P_{c(aev)} \\ \theta_s & \text{if } P_c < P_{c(aev)} \end{cases} \tag{26}$$

where S_e, θ_s, θ_r and $P_{c(aev)}$ are effective saturation degree, saturated water content, residual water content and the air-entry value of capillary pressure, respectively. The effective saturation S_e in the equation above can be written as follows:

$$S_e = \frac{\theta_m - \theta_r}{\theta_s - \theta_r}\left(1 + \left(\frac{P_c}{a}\right)^{\frac{1}{1-m}}\right)^{-m} \tag{27}$$

In particular, θ_m is the maximum water content, which is equal to or greater than the saturated water content θ_s and their values are extremely close to the COx claystone porosity of 18%. On the basis of experiments Zhang et al. (2010) and Armand et al. (2017), by fitting the water retention curve with these two experimental data (Fig. 2), the values a and m are computed for numerical simulation and listed in table 2.

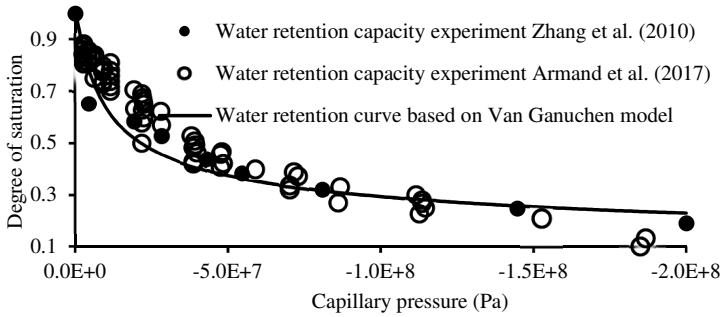

Fig. 2. Numerical water retention curve and experimental data

By imposing the effective saturation S_e=1, we can have the air-entry capillary pressure $P_{c(aev)}$ as follows:

$$P_{c(aev)} = a\left(\left(\frac{\theta_m - \theta_r}{\theta_s - \theta_r}\right)^{1/m} - 1\right)^{1-m} \tag{28}$$

where the calculated air-entry capillary pressure is lised in Table 2. However, the hydraulic conductivity k of Darcy law for unsaturated porous material is different from the one for saturated material, it is written as follow (Fachy et al., 2013):

$$k = \begin{cases} \frac{\rho g \kappa}{\mu}\kappa_R & \text{if } P_c > P_{c(aev)} \\ \frac{\rho g \kappa}{\mu} & \text{if } P_c < P_{c(aev)} \end{cases} \tag{29}$$

where κ_R is written as follows:

$$\kappa_R = \sqrt{S_e}\left(\frac{1-\left[1-\left(\frac{\theta_m - \theta_r}{\theta_s - \theta_r}S_e\right)^{1/m}\right]^m}{1-\left[1-\left(\frac{\theta_m - \theta_r}{\theta_s - \theta_r}\right)^{1/m}\right]^m}\right)^2 \tag{30}$$

All the hydraulic parameters of COx claystone for the equations above are listed in Table 2:

Table 2 Parameters for water diffusion in unsaturated COx claystone

θ_s	0.1799
θ_r	0.
θ_m	0.18
$P_{c(ave)}$ [Pa]	-1.962×10^2
$\mu[t/m*s]$	1×10^{-3}
κ_0 [m^2]	2×10^{-20}
m	0.45
a [Pa]	1.86237×10^7

3. Modeling of laboratory test

3.1 Triaxial compression tests

Under different confining stresses 0 MPa, 2 MPa, 6 MPa and 12 MPa, a series of triaxial tests on the COx claystone were carried out (Armand et al., 2017). All the tested samples were drilled from the Muse Haute-Marne underground laboratory and they were carefully protected to avoid exchanges of moisture with the outside environment and, before triaxial testing, they were equalised to a relative humidity of 90%. This relative humidity corresponds to a capillary pressure of -14 MPa, a degree of saturation of 94%, fracture energy of 10.4 N/m and tensile strength of 1.05 MPa. Fig. 3 compares the experimental and numerical results in terms of deviator stress, axial strain and lateral strain.

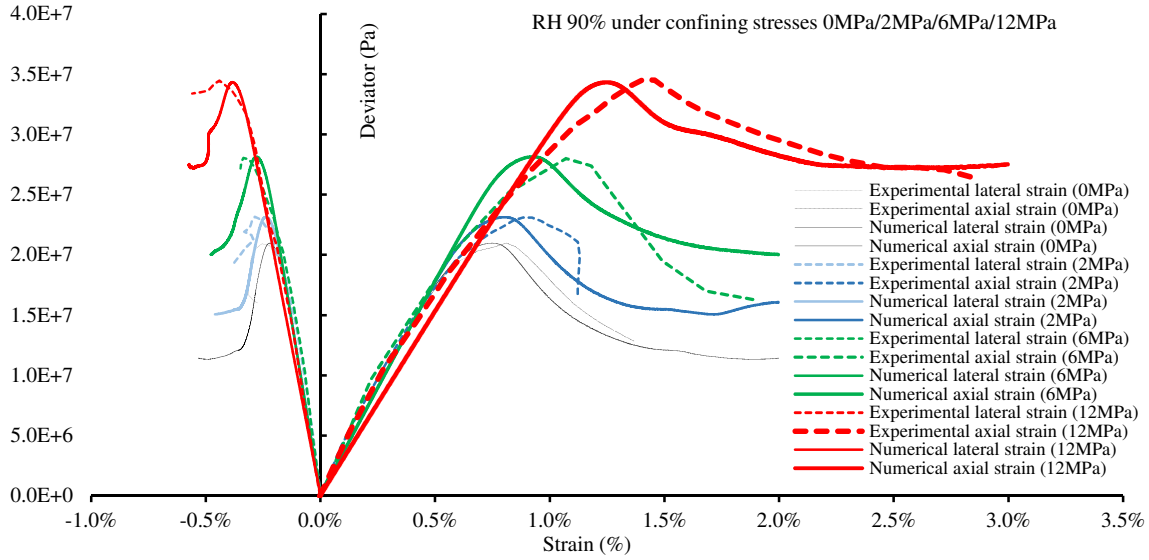

Fig. 3. Triaxial tests under confining stresses of 0 MPa/2MPa/6 MPa/12MPa at a relative humidity of 90%

The numerical simulation of the test at the confining pressure of 0 MPa (Fig. 3) shows that, in the early stages of deviatoric loading, the strain curve exhibits a linear behaviour which is consistent with experimental data. This

linear behaviour continues until the deviator stress reaches a value of about 20 MPa, at which the material response becomes nonlinear and plastic deformations occur. Moreover, the predicted peak deviator stress of 21.4 MPa matches reasonably well the measured value. As for the other triaxial tests with confining pressures of 2 MPa, 6 MPa and 12 MPa, the predicted values of peak deviator stress are 24.1 MPa, 29 MPa and 35.3 MPa, respectively, which match again reasonably well the corresponding measured values. In general, at all four levels of confining pressure, a sufficiently good fit is obtained between experimental data and model simulations.

3.2 Free desaturation/resaturation tests

The proposed model was also adopted to simulate the free deformation of the COx claystone during desaturation and resaturation paths according to the laboratory experiments carried out by Pham *et al.* (2007).

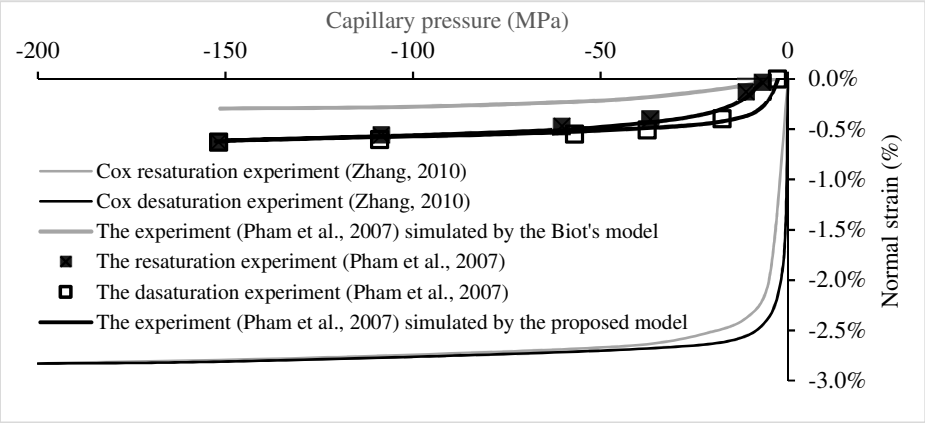

Fig. 4. Unconstrained deformations during desaturation/resaturation tests (Pham et al., 2007) and free deformation (Zhang, 2010)

Fig. 4 indicates that, when capillary pressure changes between -60 MPa and -150 MPa, the rate of deformation is relatively low. However, when capillary pressure changes between -2.7 MPa and -60 MPa, the rate of deformation increases considerably. This effect of the capillary pressure range on the deformation of the COx claystone is well captured by the proposed model, meanwhile, the numerical and experimental results validate that the significant swelling of the COx claystone mainly distributes in the capillary pressure changes between -50MPa and 0MPa.

3.3 Self-sealing of fractured COx samples by hydration

Experiments of Davy et al. (2007), Zhang (2013) and Di Donna et al. (2019) demonstrated the excellent self-sealing capability of fractured COx claystone through mechanical loading or hydration injecting synthetic water (Fig 5).

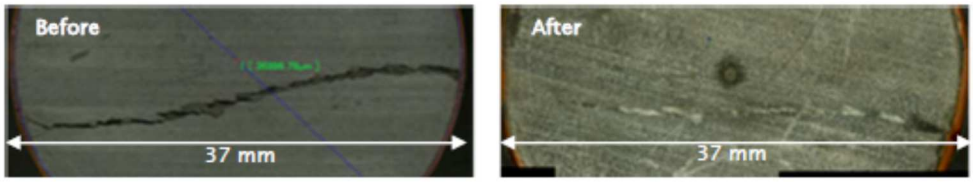

Fig. 5. The self-sealing causing by water injection

In these experiments, the macro-cracks of Callovo-Oxfordian claystone samples were created through Brazil splitting test. To analyse the impacts of the hydration and hydration time on the self-sealing of fractured COx claystone, corresponding numerical simulation for the experiments Davy et al. (2007) on the self-sealing of sample 2 MSE761 and sample 5 MSE748 are carried out, and the diffusion time of them are 5 days and 24 days, respectively. The boundary condition of theses two experiments (Davy et al., 2007): 1) Cylindrical COx samples were wraped in a special plastic films to prevent water loss, after that, brazil splitting tests were carried out to produce fractures within these samples. 2) Fractured COx samples were emplaced in a strain confined instrument to prepare for the self-sealing tests during a resaturation process, and then a water flow was loaded on their left sides of these two fractured samples. 3) Significant swelling of the material happening during the resaturation processes, fractures closing. Meanwhile, a global permeability was measured in between the left and the right sides of the fractured samples.

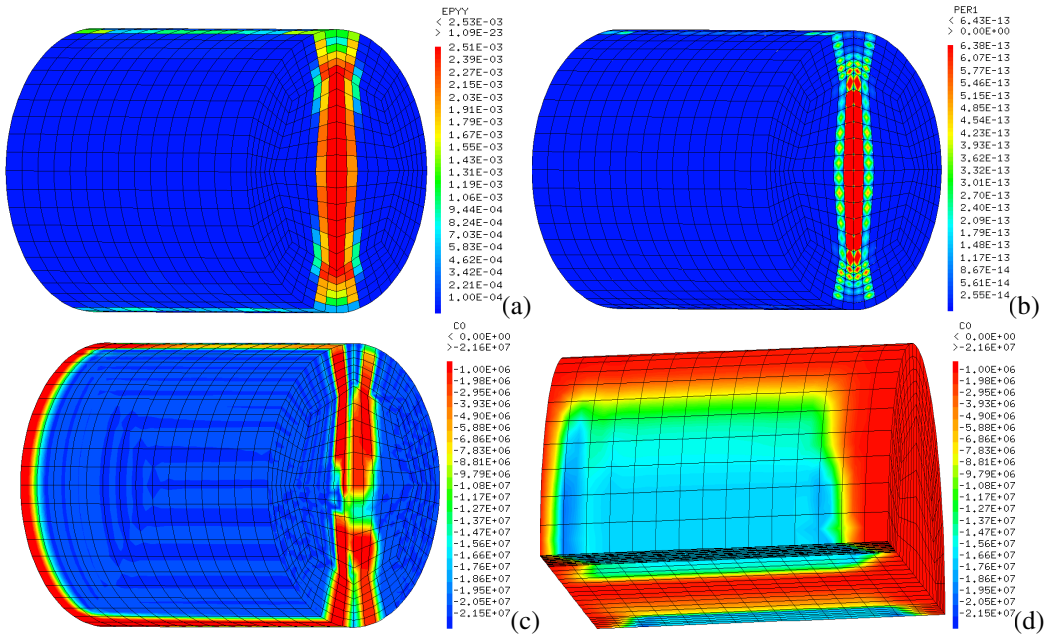

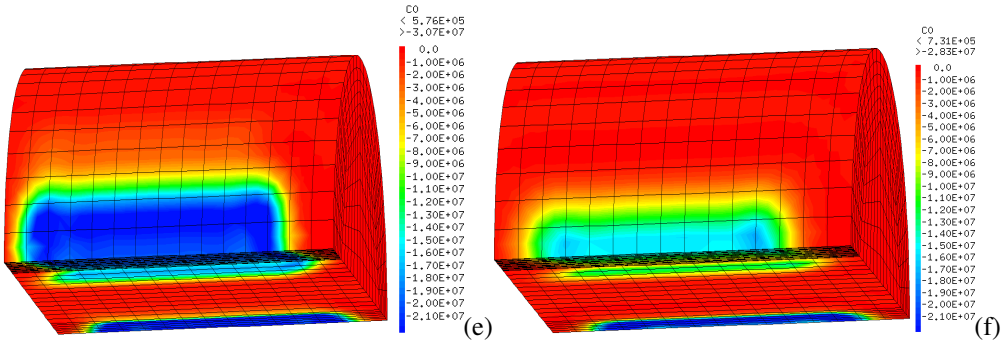

Fig. 6. (a) initial cracks value (m) of sample 2 (b) initial intrinsic permeability (m^2) of sample 2 (c) capillary pressure (Pa) of water flowing through sample 2 (d) capillary pressure of sample 2 in 5 days diffusion (e) capillary pressure of sample 5 in 12 days diffusion (f) capillary pressure of sample 5 in 24 days diffusion

Fig. 6a illustrates the value of the crack after splitting in the numerical simulation and, the corresponding intrinsic permeability resulting from these cracks displays in Fig. 6b. Fig. 6c displays the state of capillary pressure when the water flows through the macro-crack of the fractured COx claystone sample. The distribution of capillary pressure demonstrates the great difference of diffusion rate between the macro-cracked area and the intact area, which implies the large gap of the intrinsic permeability, and the increment of the intrinsic permeability accelerates the water flow dramatically. In the experiment, the process of water flow marching through the cracked cylinder was accompanied by a mechanical and chemical interaction between water and the COx claystone. It is not clear whether the chemical interaction is good for the declination of the intrinsic permeability and the self-sealing of the fractured COx claystone. Still, there is clear evidence showing that mechanical interaction produces a great swelling of COx claystone,the main reason why the fractured COx claystone could recover its impermeability and accomplish self-sealing. Same as in the experiment, the main reason of COx claystone self-sealing during the resaturation process is from the swelling of COx claystone in numerical simulation. Fig. 6d shows the capillary pressure distribution in 5 days diffusion, and the red zone (saturated zone) expands a lot in comparison with that in Fig. 6c. Fig. 6e and f show the capillary pressure of sample 5 MSE748 in 12 days and 15 days diffusion, respectively.

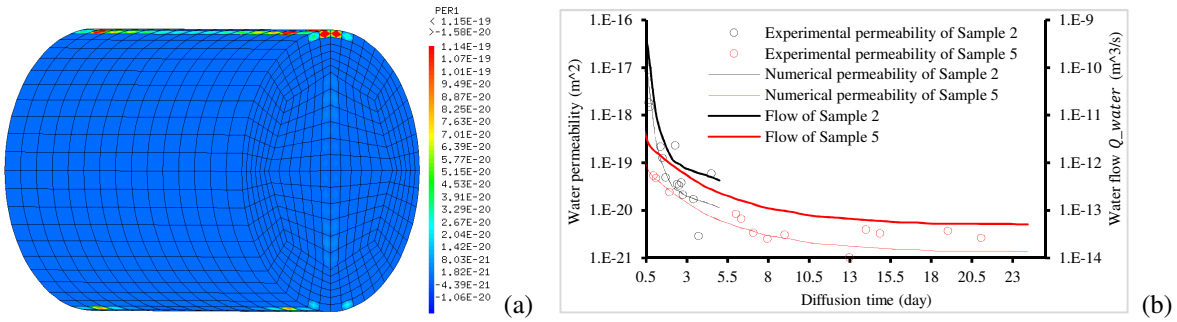

Fig. 7. (a) intrinsic permeability of sample 2 in 5 days diffusion (b) water permeability with diffusion time

Fig. 7a shows the intrinsic permeability of sample 2 in 5 days diffusion. It is clear that a significant declination occurred before and after the hydration process. Fig. 7b shows the evolutions of water permeability and water flow with the water diffusion time increment in the numerical simulation and experimental tests. In experiments, the permeability tested is an average value, whereas the permeability of numerical simulation is produced from a water flow which is calculated using intrinsic permeability in Cast3M. Examination of the numerical and experimental results indicates that both of the two cracked samples accomplish self-sealing in 0.5-day water diffusion, which validates the excellent healing property of cracked COx claystone meeting water. Comparing the permeability of sample 2 and 5 illustrates that there is a continuous reduction of permeability with the increment of diffusion time.

4. Modeling of in-situ CDZ test

In order to investigate the self-sealing of the excavation damaged zone, CDZ (Compression Damage Zone) experiment has been carried out in the Meuse/Haute-Marne underground laboratory. This experiment contains two stages: (1)measuring gas permeability during loading a pressure against the wall of underground drift, (2)measuring water permeability during a hydration process of CDZ. Fig. 8 shows the position of the drift GET in the underground laboratory where the CDZ experiment was implemented, and de La Vaissière et al. (2014, 2015) presented a detailed process of this experiment.

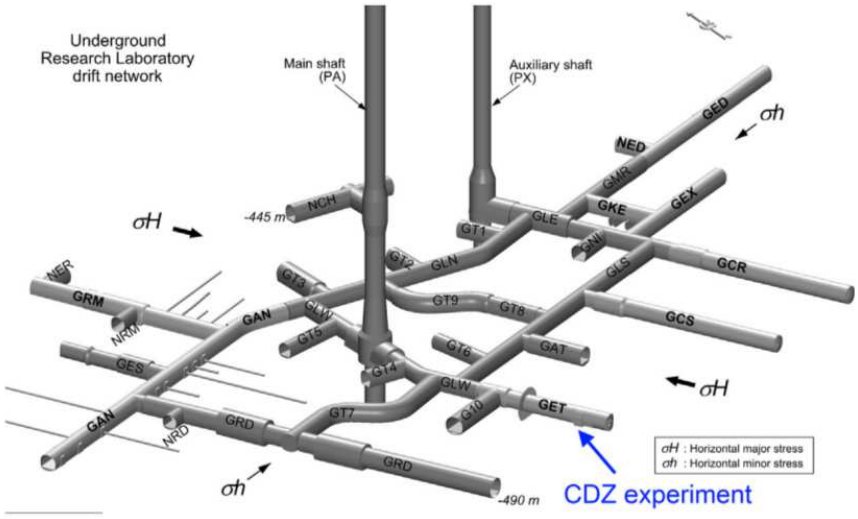

Fig. 8. Position of the drift GET for the CDZ experiment (de La Vaissière et al., 2015)

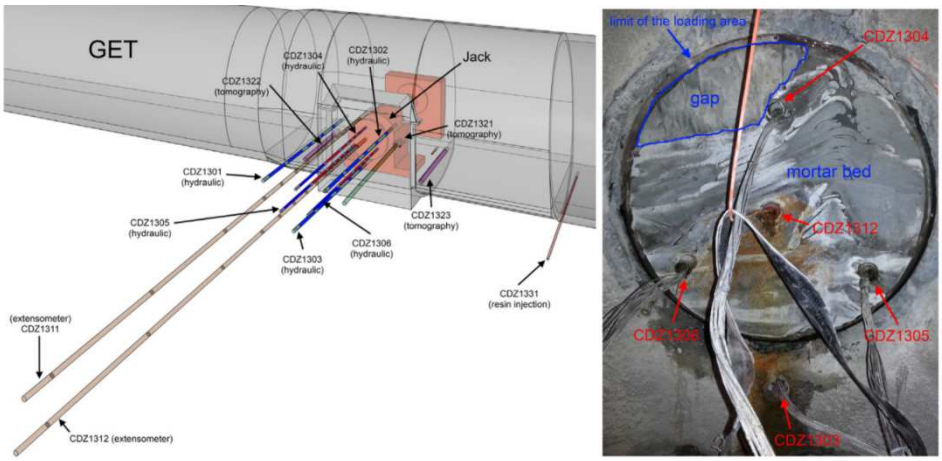

Fig. 9. Experimental setup for CDZ (de La Vaissière et al., 2015)

This drift is parallel to the major horizontal stress (σ_H) direction N150°E, the σ_H is around 16 MPa, the minor horizontal stress σ_h and the vertical stress σ_v are approximate to each other around 12.5 MPa (Wileveau et al., 2007). For the Meuse/Haute-Marne URL, if the drifts are parallel to the direction of the major horizontal stress , their excavation damage zone is mainly placed at the horizontal direction, namely, inside the walls of the drifts. Therefore, in terms of drift GET, CDZ experiment for testing self-sealing of fracture-connected zone focused on its wall sides.

Fig. 9 shows the setup for CDZ experiment. A hydraulic loading device was applied to impose a mechanical compression on the drift wall. This device consists of a 1 m^2 circular steel plate and a concrete block which was installed between the plate and the wall to reinforce the plate. Six boreholes (CDZ1301 to CDZ1306) were installed multi-packer systems for performance testing and hydraulic measurement，three of which (CDZ1301 to CDZ1303) are located near the steel plate forming an equilateral triangle with sides of 1.72 m, the other three(CDZ1304 to CDZ1306) behind the loading plate (see Fig 10). The six boreholes above hold a total surface area of 1.3 m^2 at the drift wall, and encompassed a 6.4 m^3 of the COx claystone.

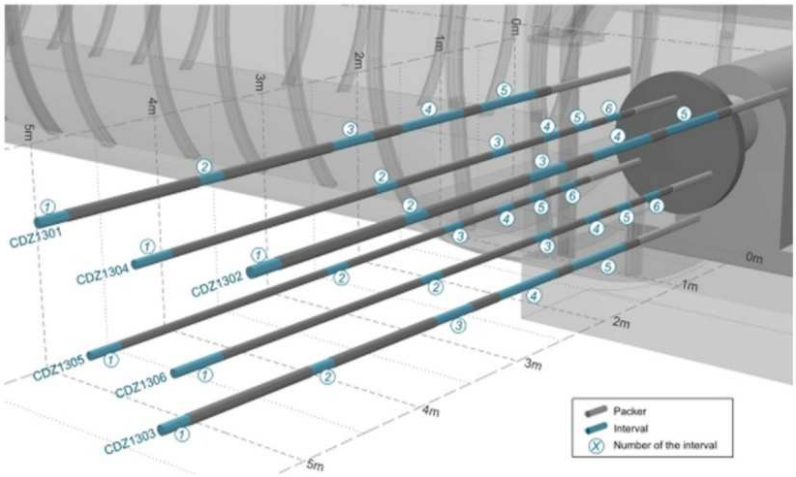

Fig. 10. Enlarged view of multi-packer boreholes (de La Vaissière et al., 2015)

Fig 10 shows an enlarged view of multi-packer boreholes. Multi-packer systems installed in the boreholes (CDZ1301 to CDZ1306) behind the plate comprise five intervals 20 cm in length except for the last interval at the end of each borehole. Between December 2010 and February 2011, all the boreholes were drilled and the installation of jack for the boreholes finished in late February 2011. To avoid the self-sealing effects of the intervals during a resaturation process after the period of installation, only intervals 1 of all the six boreholes and the intervals 2 of the boreholes (CDZ1301 to CDZ1303) were filled with synthetic water, and the rest of the intervals were filled with nitrogen at atmospheric pressure. As mentioned before, the first phase of the test is to investigate the effects of mechanical compression on the gas permeability of CDZ. This test was carried out by loading compressive pressure on the plate of increasing to 2, 3 and 4 MPa (the maximum swelling pressure providing by bentonite core against walls of drifts in the sealing system can reach 4 MPa) and then reduced to 0 MPa rapidly. These values are to selected to simulate the swelling pressure of bentonite core against the drift wall. CDZ1304, CDZ1305 and CDZ1306 were located behind the loading plate, therefore, the loading pressure was directly imposed on the zone of the three boreholes. For the second phase of investigating hydration effects, the hydration process was initiated by saturating the gas-filled intervals with synthetic water, and the hydration tests lasted one year from September 2011 to September 2012.

CDZ1301, CDZ1302 and CDZ1303 are not placed behind the loading plate, which is equal to cancel the first phase of mechanical loading, and their self-sealing directly depends on the hydration process. In CDZ experiments, self-sealing of the interval 5 of CDZ1303 (CDZ1303PRE05) by hydration was carried out, therefore the numerical simulation focus on studying self-sealing of CDZ1303PRE05 without mechanical loading in order to prove the reliability of storing nuclear waste in the COx claystone layer.

4.1 Strategy of numerical modeling for CDZ experiment

In order to approximate to the in-situ condition of CDZ experiments, a simplified method is proposed by taking the geological stresses and fracture number into account for numerical analysis. Fig 11a shows that there is a mixture between tensile and shear fractures of the cores drilled from boreholes, and Fig. 11b provides the relation between fracture density and the depth from the surface of drift wall. Based on the information of fracture patterns, fracture density and CDZ1303PRE05 position (between 0.29 m and 0.99 m from the surface of drift wall), the fracture number of CDZ1303PRE05 is 6.

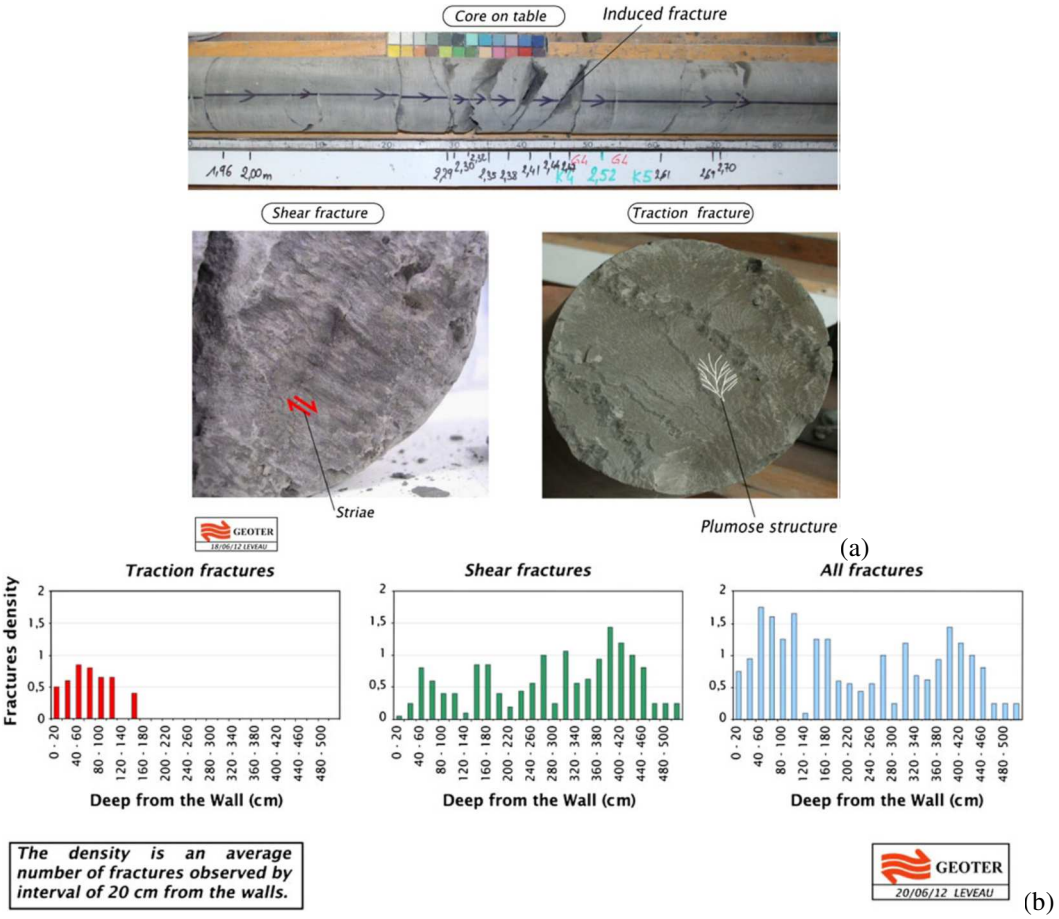

Fig. 11. Fractures density with the depth of drift sidewall (Armand et al., 2014)

Excavation induces a redistribution of geological stresses surrounding the drift, and it is not an easy task to simulate the stress condition precisely. Therefore, a simplified method is used to reproduce the stress field so that the geological stresses in numerical simulation can approximate to those of in-situ experiment, as shown in Fig. 12. Fig 12 (a) firstly shows the position of the numerical mesh for simulating the intervals of the boreholes in the CDZ experiments, the direction of the length of the numerical mesh is parallel to the intervals' direction. Secondly, a schematic for calculating the radius direction stress and tangential direction stress in the surrounding claystone of drift GET. In the CDZ experiment, the borehole (CDZ1303) is parallel to the line O_1O_2. Therefore, the tangential stress of the surrounding COx claystone of GET drift in the position of the borehole is assumed to equal to the tangential stress σ_θ along the line O_1O_2, and σ_θ is calculated using the equation (31).

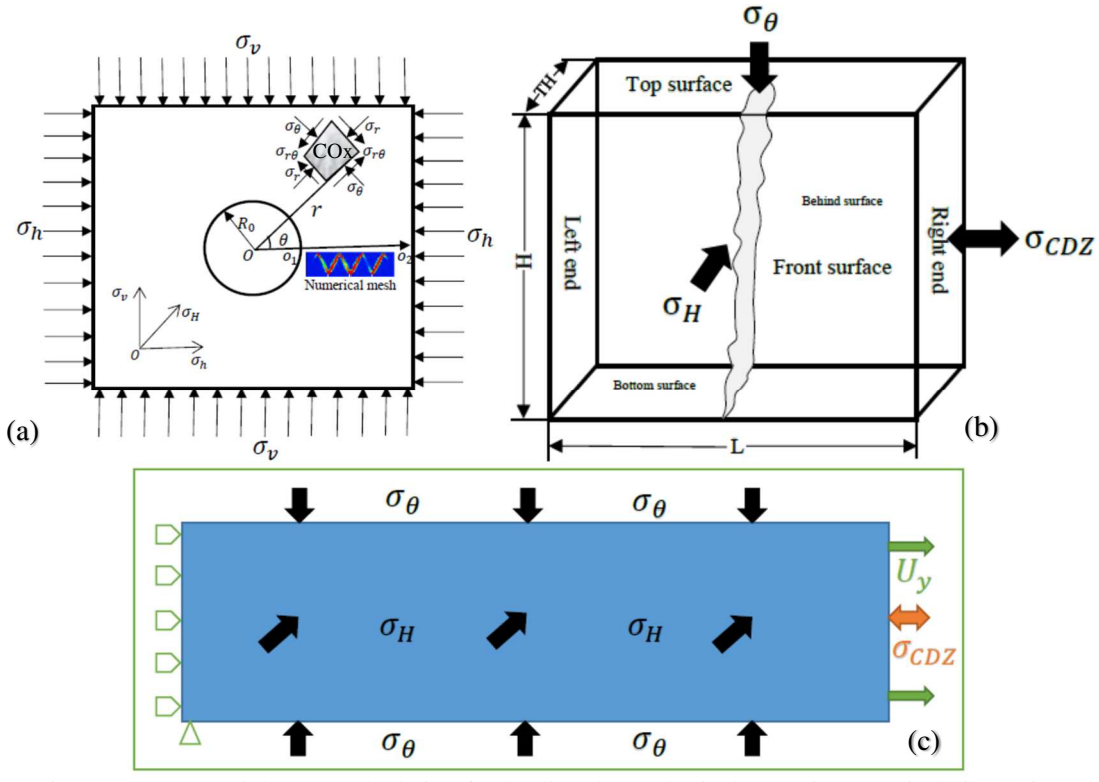

Fig. 12 (a) Tangential stress calculation for loading the geological stress in numerical simulation (b) A schematic of numerical mesh for crack opening and simulation of the CDZ experiments (c) A 2D schematic picture for boundary condition and mechanical loadings for the numerical simulation of CDZ1303PRE05

$$\sigma_\theta = \frac{\sigma_h+\sigma_v}{2}\left(1+\frac{R_0^2}{r^2}\right) - \frac{\sigma_h-\sigma_v}{2}\left(1+\frac{3R_0^4}{r^4}\right)\cos 2\theta \tag{31}$$

where $R_0 = 2.5m$, it is the radius of the drift GET. Despite the very heterogeneous orientation of the cracks observed inside the excavation damaged zone, we have simplified the approach that the simulated cracks were all parallel to the tunnel axis. Observations and measurements from Armand et al. (2014, 2017) illustrates that permeability inside tensile and shear fractures integrated zone is significantly higher than that inside shear fractures zone, therefore, the self-sealing of tensile fractures is crucial to the sealing of excavation induced fracture zone in nuclear waste disposal scheme, and this is why tensile fractures are produced in numerical model for the CDZ experiment simulation. Fig. 12 (b) shows a schematic of the numerical geometrical model for simulating the CDZ experiments, and the size of the numerical mesh includes a length of L, a height of H (0.2 m) and a depth of TH (0.1 m), and L is equal to the length of the interval of the borehole. The depth of the interval from the wall surface of GET drift and the corresponding σ_θ are listed in Table 2.

Table 3 The parameters of the interval CDZ1303PRE05 for numerical simulation

	Interval CDZ1303PRE05
Dpt	0.29m-0.99m
Fn	6
Pex	$1.04 \times 10^{-13} m^2$
σ_θ	21.2MPa

σ_H	16MPa
S_r	0.85
U_{y1}	$2.35 \times 10^{-4}m$
U_{y2}	$9.8 \times 10^{-4}m$
Pnu	$1.1 \times 10^{-13}m^2$
U_{y3}	$-2.48 \times 10^{-4}m$
U_{y4}	$2.11 \times 10^{-4}m$

Note: Dpt, Fn, Pex and Pnu are depth of intervals from gallery wall surface, fracture number, initial experimental permeability and initial numerical permeability, respectively.

The steps for the numerical simulation of CDZ1303PRE05 are listed as follows (Figure 12c):

(1) The numerical mesh is blocked on its left end.

(2) A displacement U_{y1} is loaded on the right end of the numerical mesh, and the numerical mesh is cracked from this loading. For the numerical mesh of CDZ1303PRE05, U_{y1} is $2.35 \times 10^{-4}m$.

(3) σ_θ (21.2MPa) and σ_H (16MPa) are imposed on the numerical mesh after the displacement loading. There is an displacement increasing process of the right end (ΔU_y) during the loading of σ_θ and σ_H, therefore, a displacement U_{y2} loaded on the right end whose value keeps consistent with ΔU_y so that the stress on the right end is close to 0 MPa after the two stresses loaded. $U_{y2} = \Delta U_y = 9.8 \times 10^{-4}m$.

(4) A global permeability produced by the above three steps a, b, c in numerical simulation is $1.1 \times 10^{-13}m^2$ which is approximate to the initial global permeability of $1.04 \times 10^{-13}m^2$ in CDZ experiment of CDZ1303PRE05. Therefore, the total displacement (U_y) of the right end for cracking the numerical mesh is a sum of U_{y1} and U_{y2}. $U_y = U_{y1} + U_{y2} = 1.215 \times 10^{-3}m$.

(5) Based on the above four steps, self-sealing of CDZ1303PRE05 is carried out by loading σ_{CDZ}. The method for this loading is to give a displacement U_{y3} on the right end at the opposite direction of U_{y1} and U_{y2}. When the stress on the right end reaches to 4 MPa (the maximum mechanical loading in CDZ experiments), $U_{y3} = -3.78 \times 10^{-4}m$.

(6) This step is to unload σ_{CDZ}. The method for this unloading is loading a displacement U_{y4} based on U_{y3}. When the stress on the right end comes back to 0 MPa, $U_{y4} = 2.41 \times 10^{-4}m$.

(7) After the gas permeability test, keeping σ_H, σ_θ constant, fixing the displacement of the right end, and then a hydration process is carried out by means of imposing water on the behind surface, and water flows out of the front surface through the cracks rapidly. This diffusion process lasts 100 days, and a water flow between the behind and front surface is calculated. And then a relation of a global water permeability with the diffusion time is obtained.

Due to an existed difficulty to find out a displacement U_{y1} to guarantee a obtained global permeability in numerical mesh is approximate to the initial permeability of CDZ1303PRE05 in CDZ experiment, a process of trying many times is inevitable so that an appropriate U_{y1} can be picked out.

4.2 Numerical analysis process

Strictly follow the five steps above, the numerical analysis of the self-sealing of CDZ1303PRE05 is carried out.

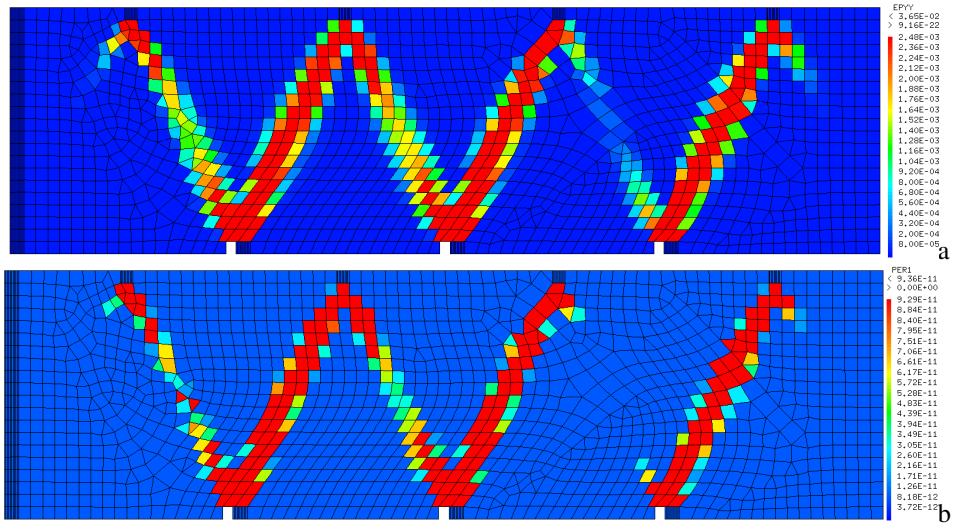

Fig. 13 (a) initial cracks value (m) of CDZ1303PRE05 (b) initial intrinsic permeability value (m^2) of CDZ1303PRE05

In the CDZ experiment, the borehole CDZ1303 is located at the outside of the steel plate, therefore the increment of the loading pressure on the steel plate had little effects on the gas permeability of CDZ1303PRE05. The global gas permeability of interval CDZ1303PRE05 was $1.04 \times 10^{-13}\ m^2$ when the loading pressure was 0 MPa, and it was $5.46 \times 10^{-14}\ m^2$with the loading pressure increased to 4 MPa. Whereas, mechanical loading directly imposed on CDZ1303PRE05 is tried in numerical simulation, and this is the advantage of the numerical method. Fig 13 shows the initial values of cracks and intrinsic permeability of CDZ1303PRE05 after steps (1) and (2).

In the numerical simulation, the initial saturation is 0.85, that is the same as in the experiment, and the corresponding capillary pressure at this saturation is$-2.15 \times 10^{7} Pa$. With the increment of σ_{CDZ}, a method is taken to calculate a mean permeability using intrinsic permeability. The method is to imposing a gas pressure p1 on the front surface and another gas pressure p2 on the behind surface. This gas pressure difference (p1-p2) provides a gas flow between the two surfaces, the equation for flow calculation is shown as follow:

$$Q_{gas} = \iint q_{gas} ds \tag{40}$$

Based on the gas flow Q_{gas}, the global gas permeability is calculated as follow:

$$\kappa_{gas} = \frac{2\times(2.2\times10^{-5}Pa*s)\times(1.01\times10^{5}Pa)\times(1\times10^{-1}m)Q_{gas}}{(0.7m*0.2m)((1.5\times10^{6}Pa)^2-(1.01\times10^{5}Pa)^2)} \tag{41}$$

With the growth of the compression pressure, the cracks close and the intrinsic permeability decreases. Therefore, the gas flow Q_{gas} which is calculated from CAST3M decreases at the same time, and the corresponding global gas permeability κ_{gas} also decreases, which are displayed in Fig. 14.

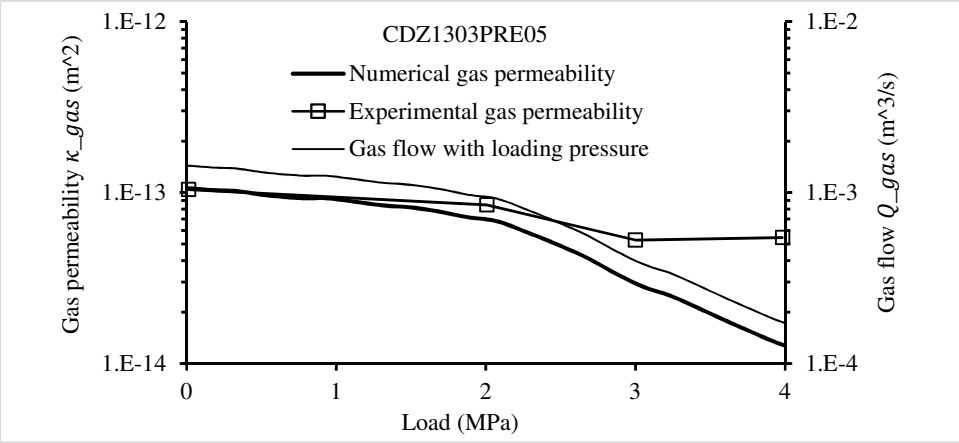

Fig. 14. Permeability change with loading pressure

Fig. 14 shows that the gas permeability decreases from $1.04 \times 10^{-13} m^2$ to $1.2 \times 10^{-14} m^2$ with the loading pressure increases from 0 MPa to 4 MPa in the numerical simulation. The difference between the experimental and numerical results when loading pressure is 4 MPa illustrates that the mechanical loading makes a significant contribution to the decrease of the global gas permeability.

For the hydration process of CDZ1303PRE05, we assumed that there is no mechanical load imposed in numerical simulation. Therefore, the initial global permeability for hydration is numerically beginning from $1.1 \times 10^{-13} m^2$. The hydro-mechanical behaviors occurred in the hydration process both of the experimental and numerical methods include:

(1) Water was injected in the gas-filled interval CDZ1303PRE05 in the experiment. In the numerical simulation, capillary pressure of the behind surface of the numerical mesh is decreased from $-2.15 \times 10^7 Pa$ to $0\ Pa$, and a diffusion process begins.

(2) In the experiment, interval 5 of CDZ1303 was filled with water and water diffusion occurred in the surrounding area of the interval. This diffusion included water penetrating in intact COx claystone and water flowing through fractures. In the numerical simulation, capillary pressure starts to vary due to the capillary pressure gradient between the behind surface of the cuboid and its rest parts, the variation rate is determined by the intrinsic permeability which is summed up by the initial permeability of intact COx and the permeability from cracks.

(3) In the experiment, the interaction between water and COx led to swelling and the cracks closure during the resaturation process. This swelling closed water pathway, and it slowed down the rate of water diffusion. In the numerical simulation, the variation of capillary pressure produces deformation, which decreases the width of cracks (Fig. 13a) and permeability (Fig. 13b).

Fig. 15a numerically demonstrates the saturated and unsaturated parts in 0.1-day water diffusion. If the six main cracks in Fig. 15a are numbered 1- 6 from the left to the right side, we can find that water flows through the second crack at the first moment due to its high permeability, that is why the place of the second crack has the largest saturated zone (the red area). In the experiment, the depth of the cracked COx for water diffusion could be regarded as an infinitive, and the corresponding one in numerical simulation is 0.1 m. Therefore, water will completely flow out of all the six cracks by turns and, and finally, all the material will be saturated. Fig. 15b illustrates the saturated zone in one-day diffusion. In comparison with the one in 0.1-day diffusion, there is a significant expansion of the red zone, and the expansion in the second crack zone is more evident due to the well-developed micro-cracks in this part. Fig. 15c displays the distribution of the saturated and unsaturated zone in 10 days diffusion. It is clear that water flows out of all the main cracks except for the fifth main crack. Fig. 15d shows the proportion between the saturated zone and unsaturated zone in 100 days diffusion, and there are 70% of the mesh saturated. Due to the extremely low permeability of the intact COX, there are 30% area unsaturated remained.

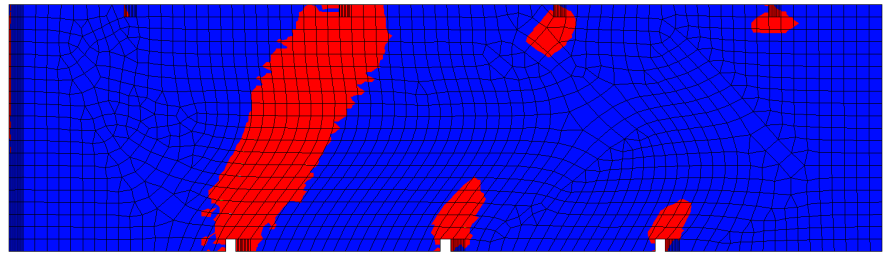

(a)

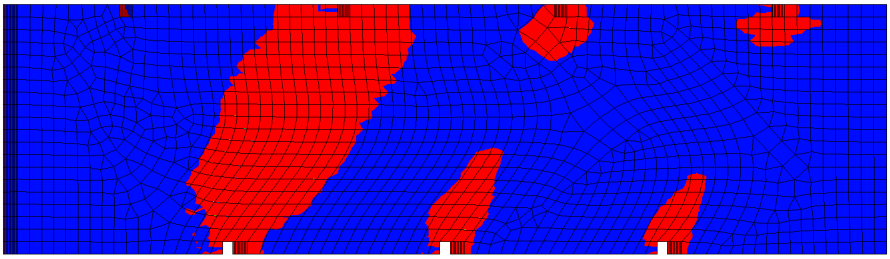

(b)

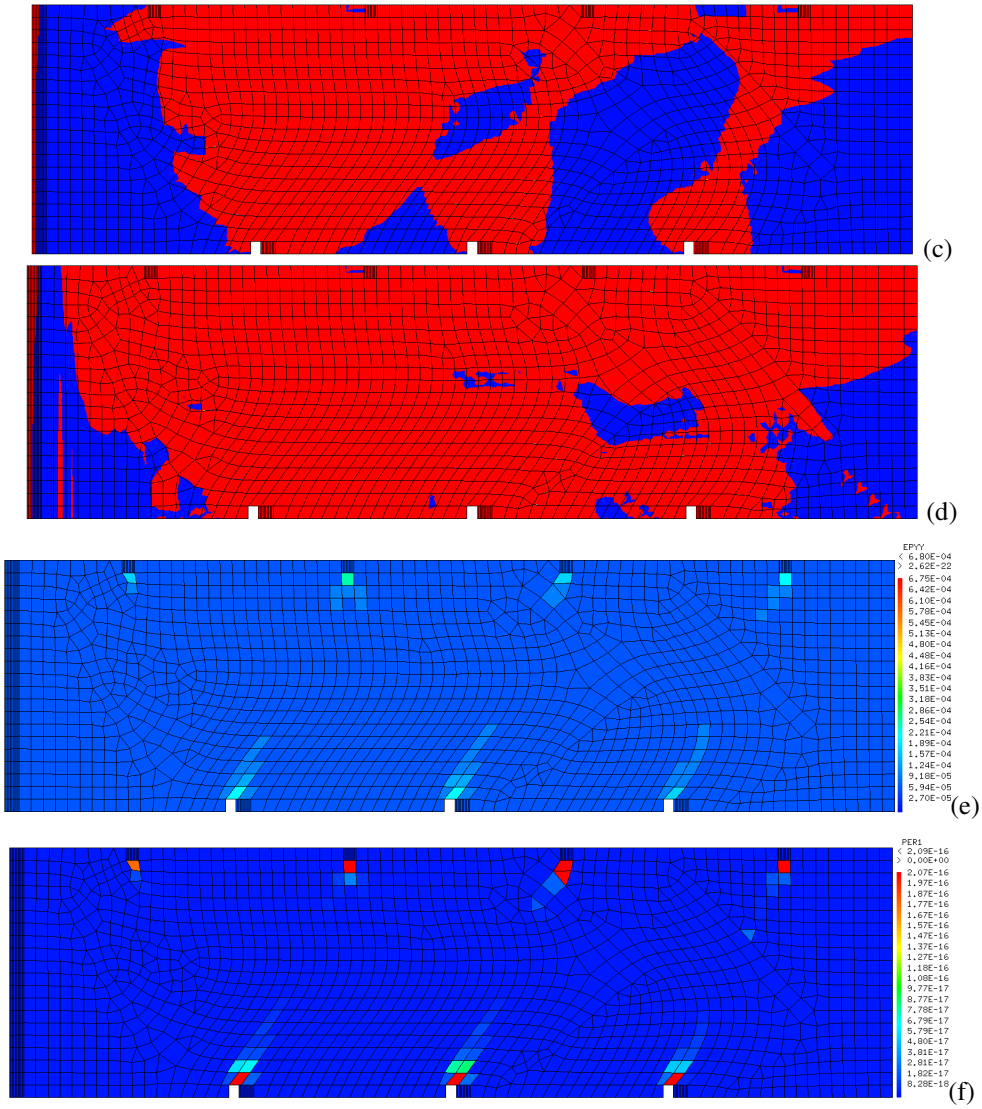

Fig. 15 Saturated zone *(the red area)* (a) 0.1 day diffusion (b) 1 day diffusion (c) 10 days diffusion (d) 100 days diffusion (e) initial cracks value of CDZ1303PRE05 in 100 days diffusion (f) initial intrinsic permeability value of CDZ1303PRE05 in 100 days diffusion

In comparison with the cracks value before the resaturation process, there is a significant declination of this value after 100 days resaturation (Fig. 15e). This declination proves the self-sealing capacity of cracked COx during the resaturation process.

In terms of the maximum intrinsic permeability, the value is $9.36 \times 10^{-11}\ m^2$ before the resaturation process, whereas it declines to $2.09 \times 10^{-16} m^2$ in 100 days resaturation (Fig. 15f). Moreover, the maximum intrinsic permeability mainly placed at the positions of notches. Therefore, there would be a significant decrease when the intrinsic permeability is transferred into the global water permeability.

To calculate the global water permeability, a water flow Q_{water} is calculated in CAST3M according to the following equation and its relation with the diffusion time is shown in Fig. 16.

$$Q_{water} = \iint q_{water} ds \tag{42}$$

Substituting the water flow Q_{water} into the following equation

$$\kappa_{water} = \frac{\mu_w L Q_{water}}{A(P_1 - P_2)} \tag{43}$$

where $\mu_w = 1.005 \times 10^{-3}\, Pa * s$ and $P_1 = 1.5 MPa, P_2 = 0.1\, MPa$, A = 0.2x 0.7 (m2) and TH = 0.1 m. Through this calculation, the global water permeability of the cracked material between the behind and the front surface is shown as following:

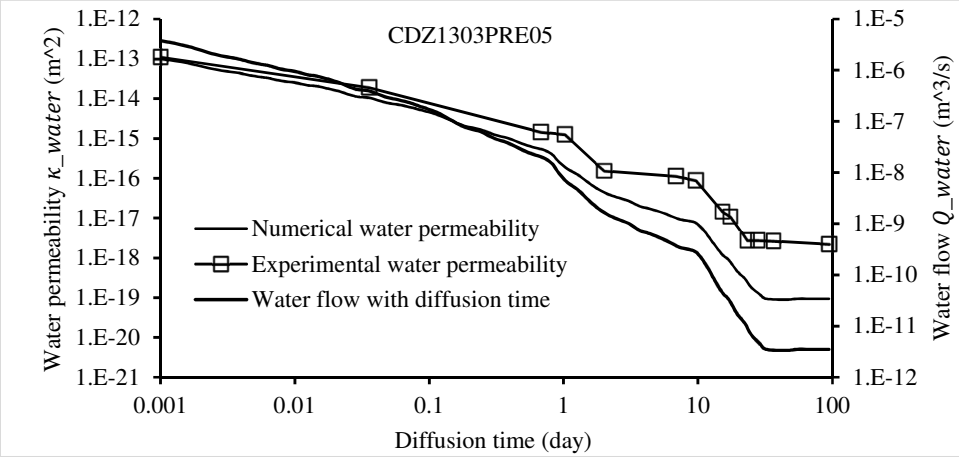

Fig. 16 Permeability change with diffusion time

Fig. 16 shows the changes of the experimental water permeability, numerical water permeability and water flow with the increment of the diffusion time. Inspection of this Fig. 16 illustrates that the minimum values both of the numerical and experimental water permeability are less than $1 \times 10^{-17} m^2$, t proving that the cracked zone of CDZ1303PRE05 can accomplish self-sealing without an extra compression pressure loaded. The initial global water permeability is $1.04 \times 10^{-13} m^2$ in the experiment, and the corresponding value is $1.1 \times 10^{-13} m^2$ in the numerical simulation. This value of the experiment decreased to $2.28 \times 10^{-18} m^2$ in 100 days diffusion, and the corresponding value of the numerical simulation declines to $1.13 \times 10^{-19} m^2$. The most significant declination of the water permeability was obtained in one-day diffusion due to the swelling of COx claystone during the hydration process. And the proposed model captured this behaviour perfectly with the declination of the water permeability to $2.1 \times 10^{-16} m^2$ after one-day diffusion. This declination of permeability slows down the water diffusion in the later period, and it contributes significant effects on the self-sealing of the fractured material. The accomplishment of the self-sealing of CDZ1303PRE05 proves that the excavation induced fracture zone can recover to its initial permeability even there was no mechanical loading imposed on the drift wall. The good agreement between the numerical and experimental results validates that the proposed model can analyse the large scale self-sealing in the underground excavated damage zone. The bentonite backfill to underground galleries after the emplacement of nuclear waste will provide a great loading pressure against the galleries' walls

due to the excellent swelling capacity of bentonite in a later resaturation process, which will further strength the self-sealing of the excavated damage zone.

5. Conclusion

To model the hydro-mechanical behaviour of Callovo-Oxfordian claystone, an elastoplastic damage model coupled with an added deformation upon saturation model in the framework of Biot theory is proposed in the present paper. The model accounts for the variation of Young's modulus, tensile strength and fracture energy with capillary pressure change and is able to represent the mechanical behaviour of claystone under different saturation and stress conditions. Because the standard Biot's theory is not able to exhibit the significant shrinkage/swelling deformation of COx claystone due to the variation of water content, a hysteretic model that accounts for this "extra deformation" is proposed, and this model can simulate COx claystone swelling with water content changing under free or confined conditions.

Due to the necessity of describing the self-sealing of fractures connected zone and fractures diffuse zone, cracks estimation is carried out by a post-processing method based on fracture energy regularization, and then permeability evaluation is carried out by introducing the estimated cracks value into the Cubic law. In this paper, the self-sealing of fractured COx claystone samples and the self-sealing of CDZ experiments are analysed using the numerical method in terms of the quantities of cracks and permeability. For the self-sealing of fractured COx claystone samples, water permeability can easily decline to less than $1 \times 10^{-17} m^2$ when water flows through cracks of COx claystone, and an evident cracks closure process was observed in experiments due to the induced swelling of COx claystone. The declination of permeability is also obtained in numerical simulation, and good agreements between the numerical and experimental results illustrate that the self-sealing of fractured COx claystone samples and fracture-connected zone can accomplish. In comparison with experiments of the self-sealing of fractured COx claystone which can only test an average permeability, the numerical simulation of the proposed model can detail the anisotropic intrinsic permeability evolution which provides us a better understanding of the mechanism of the self-sealing of cracked COx claystone. Based on the perfect performance of this model in describing self-sealing of cracked COx claystone samples, the numerical simulation and experimental test of self-sealing of CDZ1303PRE05 prove that the fracture-connected zone can seal by hydration, whereas there will be bentonite cores put in the sealing system in engineering application which is able to provide a maximum stress of 4 MPa against the wall of fracture-connected zone. Therefore, the safety for storing nuclear waste in Cigéo underground drift of France can be guaranteed.

In conclusion, a new model which can describe the hydro-mechanical behaviors of excavated damage zone in French nuclear waste deep disposal scheme was developed. It is also the first time that a numerical analysis method is successfully used to simulate the time-dependent self-sealing of fractured unsaturated claystone by a hydration process. The application of the new model can expand to analyse the hydro-mechanical behaviors of other claystone which are similar to COx claystone, such as Opalinus claystone and Boom clay.

Acknowledgements

The authors gratefully acknowledge the funding by the French National Radioactive Waste Management Agency (Andra) and China Scholarship Committee (CSC).

References

Armand, G., Bumbieler, F., Conil, N., de la Vaissière, R., Bosgiraud, J.M., Vu, M.N. (2017). Main outcomes from in situ thermo-hydro-mechanical experiments programme to demonstrate feasibility of radioactive high-level waste disposal in the Callovo-Oxfordian claystone. Journal of Rock Mechanics and Geotechnical Engineering 9 (3), 415-427

Armand, G., Conil, N., Talandier, J. and Seyedi, D.M., 2017. Fundamental aspects of the hydromechanical behaviour of Callovo-Oxfordian claystone: from experimental studies to model calibration and validation. Computers and Geotechnics, 85, pp.277-286.

Armand, G., Leveau, F., Nussbaum, C., de La Vaissiere, R., Noiret, A., Jaeggi, D., Landrein, P. and Righini, C., 2014. Geometry and properties of the excavation-induced fractures at the Meuse/Haute-Marne URL drifts. Rock Mechanics and Rock Engineering, 47(1), pp.21-41.

Assadollahi, H., Nowamooz, H. (2020). Long-term analysis of the shrinkage and swelling of clayey soils in a climate change context by numerical modelling and field monitoring. Computers and Geotechnics, 127, 103763.

Biot, M.A., 1941. General theory of three‐dimensional consolidation. Journal of applied physics, 12(2), pp.155-164.

Darde, P Dangla, JN Roux, JM Pereira, J Talandier, MN Vu, AM Tang (2020) Modelling the behaviour of bentonite pellet-powder mixtures upon hydration from dry granular state to saturated homogeneous state. Engineering Geology (in press)

Cast3M: http://www-cast3m.cea.fr/

Conil, N., Vitel, M., Plua, C. et al. In Situ Investigation of the THM Behavior of the Callovo-Oxfordian Claystone. Rock Mech Rock Eng 53, 2747–2769 (2020). https://doi.org/10.1007/s00603-020-02073-8

Davy, C.A., Skoczylas, F., Barnichon, J.D. and Lebon, P., 2007. Permeability of macro-cracked claystone under confinement: gas and water testing. Physics and Chemistry of the Earth, Parts A/B/C, 32(8-14), pp.667-680.

De La Vaissière, R., Morel, J., Noiret, A., Côte, P., Helmlinger, B., Sohrabi, R., Nussbaum, C. (2014). Excavation-induced fractures network surrounding tunnel: properties and evolution under loading. Geological Society, London, Special Publications, 400(1), 279-291.

De La Vaissière, R., Armand, G. and Talandier, J., 2015. Gas and water flow in an excavation-induced fracture network around an underground drift: a case study for a radioactive waste repository in clay rock. Journal of Hydrology, 521, pp.141-156.

Descostes, M., Blin, V., Bazer-Bachi, F., Meier, P., Grenut, B., Radwan, J., ... & Tevissen, E. (2008). Diffusion of anionic species in Callovo-Oxfordian argillites and Oxfordian limestones (Meuse/Haute–Marne, France). Applied Geochemistry, 23(4), 655-677.

Diederichs, M. S. (2003). Manuel rocha medal recipient rock fracture and collapse under low confinement conditions. Rock Mechanics and Rock Engineering, 36(5), 339-381.

Di Donna, A., Charrier, P., Salager, S., Bésuelle, P. (2019). Self-sealing capacity of argillite samples. In E3S Web of Conferences (Vol. 92, p. 03005). EDP Sciences.

Fahy, C., Gallipoli, D. and Grassl, P., 2013. A lattice model for liquid transport in unsaturated porous materials. In Advances in Unsaturated Soils (pp. 525-530). CRC Press.

Fichant, S., La Borderie, C. and Pijaudier-Cabot, G., 1999. Isotropic and anisotropic descriptions of damage in concrete structures. Mechanics of Cohesive-frictional Materials: An International Journal on Experiments, Modelling and Computation of Materials and Structures, 4(4), pp.339-359.

Fouché, O., Wright, H., Le Cléac'h, J.M. and Pellenard, P., 2004. Fabric control on strain and rupture of heterogeneous shale samples by using a non-conventional mechanical test. Applied Clay Science, 26(1-4), pp.367-387.

F Zhang, YJ Cui, N Conil, J Talandier (2020). Effect of fracture voids on the swelling behaviour of Callovo-Oxfordian claystone. Engineering Geology (in press).

Gens, A. and Alonso, E.E., 1992. A framework for the behaviour of unsaturated expansive clays. Canadian Geotechnical Journal, 29(6), pp.1013-1032.

Giot R, Auvray C, Conil N, de La Vaissière (2018). Multi-stage water permeability measurements on claystone by steady and transient flow method. Engineering Geology 247: 27-37

Gong, Y., Chok, Y. H. (2018). Predicted and measured behaviour of a test embankment on Ballina clay. Computers and Geotechnics, 93, 178-190.

Grasberger, S. and Meschke, G., 2004. Thermo-hygro-mechanical degradation of concrete: From coupled 3D material modelling to durability-oriented multifield structural analyses. Materials and Structures, 37(4), pp.244-256.

Huang, Z., Jiang, Z., Zhu, S., Wu, X., Yang, L. and Guan, Y., 2016. Influence of structure and water pressure on the hydraulic conductivity of the rock mass around underground excavations. Engineering Geology, 202, pp.74-84.

He, Y., Ye, W. M., Chen, Y. G., Zhang, K. N., Wu, D. Y. (2020). Effects of NaCl solution on the swelling and shrinkage behavior of compacted bentonite under one-dimensional conditions. Bulletin of Engineering Geology and the Environment, 79(1), 399-410.

Li, L., Li, J., Sun, D. A. (2016). Anisotropically elasto-plastic solution to undrained cylindrical cavity expansion in K0-consolidated clay. Computers and Geotechnics, 73, 83-90.

Liu, Y., Vanapalli, S. K. (2019). Load displacement analysis of a single pile in an unsaturated expansive soil. Computers and Geotechnics, 106, 83-98.

Matallah, M. and La Borderie, C., 2009. Inelasticity–damage-based model for numerical modeling of concrete cracking. Engineering Fracture Mechanics, 76(8), pp.1087-1108.

Matallah, M. and La Borderie, C., 2016, May. 3D numerical modeling of the crack-permeability interaction in fractured concrete. In 9th International Conference on Fracture Mechanics of Concrete and Concrete Structures (FraMCoS-9) Saouma V, Bolander J, Landis E, eds. Berkeley, USA.

Pham, Q.T., Vales, F., Malinsky, L., Minh, D.N. and Gharbi, H., 2007. Effects of desaturation–resaturation on mudstone. Physics and Chemistry of the Earth, Parts A/B/C, 32(8-14), pp.646-655.

Pardoen, B., Talandier, J., & Collin, F. (2016). Permeability evolution and water transfer in the excavation damaged zone of a ventilated gallery. International Journal of Rock Mechanics and Mining Sciences, 85, 192-208.

Qi, S., Vanapalli, S. K. (2016). Influence of swelling behavior on the stability of an infinite unsaturated expansive soil slope. Computers and Geotechnics, 76, 154-169.

Rastiello, G., Boulay, C., Dal Pont, S., Tailhan, J.L. and Rossi, P., 2014. Real-time water permeability evolution of a localized crack in concrete under loading. Cement and Concrete Research, 56, pp.20-28.

Secchi, S. and Schrefler, B.A., 2012. A method for 3-D hydraulic fracturing simulation. International journal of fracture, 178(1-2), pp.245-258.

Souley M, Vu MN, Armand G. 3D anisotropic modelling of deep drifts at the Meuse/Haute-Marne URL. 5th Int. Itasca Symp., Vienna, Austria.: 2020

Trivellato, E., Pouya, A., Vu, M.N, & Seyedi, D. (2019). A softening damage-based model for the failure zone around deep tunnels in quasi-brittle claystone. Tunnels and Underground Cities. Engineering and Innovation Meet Archaeology, Architecture and Art, pp 4242-4251, CRC Press.

Van Genuchten, M.T., 1980. A closed-form equation for predicting the hydraulic conductivity of unsaturated soils. Soil science society of America journal, 44(5), pp.892-898.

Vogel, T., Gerke, H.H., Zhang, R. and Van Genuchten, M.T., 2000. Modeling flow and transport in a two-dimensional dual-permeability system with spatially variable hydraulic properties. Journal of hydrology, 238(1-2), pp.78-89.

Volckaert, G., Bernier, F., Sillen, X., Van Geet, M., Mayor, J.C., Göbel, I., Blümling, P., Frieg, B., Su, K. and ANDRA, F., 2004. Similarities and differences in the behaviour of plastic and indurated clays. Proceedings of Euradwaste, 4.

Vu MN, Guayacán-Carrillo LM, Armand G (2020) Excavation induced over pore pressure around drifts in the Callovo-Oxfordian claystone. European Journal of Environmental and Civil Engineering. DOI: 10.1080/19648189.2020.1784800.

Vinsot, A., Leveau, F., Bouchet, A., & Arnould, A. (2014). Oxidation front and oxygen transfer in the fractured zone surrounding the Meuse/Haute-Marne URL drifts in the Callovian–Oxfordian argillaceous rock. Geological Society, London, Special Publications, 400(1), 207-220.

Wang Q, Tang AM, Cui YJ, Delage P, Gatmiri B. Experimental study on the swelling behaviour of bentonite/claystone mixture. Engineering Geology.Volume 124, 4 January 2012, Pages 59-66

Witherspoon, P.A., Wang, J.S., Iwai, K. and Gale, J.E., 1980. Validity of cubic law for fluid flow in a deformable rock fracture. Water resources research, 16(6), pp.1016-1024.

Wileveau, Y., Cornet, F.H., Desroches, J. and Blumling, P., 2007. Complete in situ stress determination in an claystone sedimentary formation. Physics and Chemistry of the Earth, Parts A/B/C, 32(8-14), pp.866-878.

Yin, Z.Y., Jin, Y.F., Shen, J.S. and Hicher, P.Y., 2018. Optimization techniques for identifying soil parameters in geotechnical engineering: comparative study and enhancement. International Journal for Numerical and Analytical Methods in Geomechanics, 42(1), pp.70-94.

Zhang, C.L., Wieczorek, K. and Xie, M.L., 2010. Swelling experiments on mudstones. Journal of Rock Mechanics and Geotechnical Engineering, 2(1), pp.44-51.

Zhang, C.L., 2013. Sealing of fractures in claystone. Journal of Rock Mechanics and Geotechnical Engineering, 5(3), pp.214-220.

Zhang CL, Armand G, Conil N, Laurich B (2019). Investigation on anisotropy of mechanical properties of Callovo-Oxfordian claystone. Engineering Geology 251: 128-145

Zhang, F., Jia, Y., Bian, H.B. and Duveau, G., 2013. Modeling the influence of water content on the mechanical behavior of Callovo–Oxfordian claystone. Physics and Chemistry of the Earth, Parts A/B/C, 65, pp.79-89.

Zhang, F., Cui, Y., Conil, N. et al. Assessment of Swelling Pressure Determination Methods with Intact Callovo-Oxfordian Claystone. Rock Mech Rock Eng 53, 1879–1888 (2020).https://doi.org/10.1007/s00603-019-02016-y

Zhou, H., Liu, H., Zha, Y., Yin, F. (2017). A general semi-analytical solution for consolidation around an expanded cylindrical and spherical cavity in modified Cam Clay. Computers and Geotechnics, 91, 71-81.